Elastic proton scattering from ^{4}He at 297 MeV

M. Yoshimura,[1,*] M. Nakamura,[1] H. Akimune,[2,†] I. Daito,[2,‡] T. Inomata,[3,§] M. Itoh,[1] M. Kawabata,[2,‖] T. Noro,[2]
H. Sakaguchi,[1] H. Takeda,[1] A. Tamii,[1,¶] K. Yonehara,[4] H. P. Yoshida,[2] and M. Yosoi[1,*]

[1]*Department of Physics, Kyoto University, Kyoto 606-8502, Japan*
[2]*Research Center for Nuclear Physics, Osaka University, Ibaraki, Osaka 567-0047, Japan*
[3]*Department of Physics, Osaka University, Toyonaka, Osaka 560-0043, Japan*
[4]*Department of Physics, Konan University, Kobe, Hyogo 658-8501, Japan*
(Received 15 October 2000; published 22 February 2001)

Differential cross sections, analyzing powers, and spin rotation parameters for elastic scattering of protons on ^{4}He at 297 MeV have been measured over a wide angular range ($12° \leq \theta_{lab} \leq 66°$). Experimental data have been microscopically analyzed with relativistic impulse approximation calculations. The spin observables up to medium scattering angles ($\theta_{c.m.} \leq 40°$) are predominantly sensitive to the ratio of the volume integral of scalar density to vector density. With a ratio of 0.92, which is significantly smaller than those for heavier nuclei (0.96–0.98), both spin observables as well as the differential cross section have been quantitatively reproduced. According to nuclear matter calculations, the small ratio reflects a high mass density. At backward angles, the experimental cross sections are larger than any of the values calculated with realistic density distributions.

I. INTRODUCTION

Elastic scattering of polarized protons on nuclei at intermediate energies is a suitable tool for providing important information on nucleon-nucleon (NN) interactions, wave functions of the target nucleus, and reaction mechanisms. Therefore, many studies of proton elastic scattering have been performed on various targets and for a broad range of beam energies. It is known that at incident energies of several hundred MeV, the total NN cross section has a minimum and the nuclear reaction is expected to be well described by a direct reaction mechanism. In this energy region, the NN interaction itself has been investigated in detail by NN scattering [1]. At laboratory beam energies of 200 MeV, 300 MeV, and 400 MeV, Horowitz *et al.* [2,3] parametrized the NN interaction in the Lorentz invariant form of the NN amplitude with a relativistic Love-Franey model. Murdock and Horowitz [3] have calculated observables for proton elastic scattering with a relativistic impulse approximation (RIA) using these parameter sets of the NN interaction. They have succeeded in describing quite well the observables, especially the analyzing power A_y and the spin rotation parameter Q, for several targets from ^{12}C to ^{208}Pb. However, they did not consider ^{4}He because of the expected

large center-of-mass (c.m.) corrections, which were not included in their RIA formalism. Whether the RIA with an appropriate recoil correction can be applied to light nuclei as ^{4}He or not is still open to question.

^{4}He is the smallest closed shell nucleus. Its density or wave function has been extensively studied both experimentally and theoretically. The measured small root-mean-square (rms) charge radius obtained from electron scattering [4] suggests that the mass density in the center of the ^{4}He nucleus is much higher than the ''normal'' density. Moreover, there are calculations which predict a central mass density of the ^{4}He nucleus twice the ''normal'' density. Examples are the calculations for the four-body ^{4}He system using the ATMS (amalgamation of two-body correlations into the multiple scattering process) wave function generated with the Reid soft core V_8 potential [5] and the Green function Monte Carlo (GFMC) calculations [6] using a variety of nucleon-nucleon interactions.

During the past more than 20 years, p-^{4}He elastic scattering has been widely measured at various energies in the intermediate energy region [7]. Arnold *et al.* systematically analyzed the data of differential cross section $d\sigma/d\Omega$ and the analyzing power A_y above 500 MeV incident beam energy with a phenomenological Dirac optical potential and obtained a qualitative fit of the A_y, which is poorly described by the Schrödinger equation [8,9]. The energy dependence of the ratio of the volume integral of the scalar potential to the vector potential was investigated. However, the spin rotation parameter Q was not included in their analyses because there were no data. Elastic scattering of protons (spin 1/2) on spin 0 targets has only three independent observables: $d\sigma/d\Omega$, A_y, and one of the spin rotation parameters [10]. The spin rotation parameter R for proton elastic scattering on ^{4}He was measured first at an incident energy of $E_p = 500$ MeV [11]. It was reported that the ambiguity of the phenomenological optical potential was much reduced by adding the spin rotation parameter to the data of $d\sigma/d\Omega$ and A_y [12,13]. Since statistical errors of the measured R parameters, however,
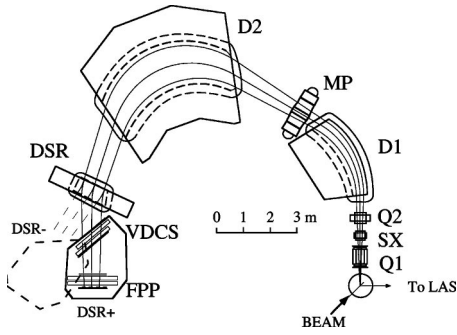
FIG. 1. Layout of the Grand Raiden spectrometer and the focal-plane detector system. The detectors are shown in the DSR+ mode. For measurements in the DSR− mode indicated by dashed lines, the detectors were moved to the other focal plane.

were large, especially at backward angles, some potential ambiguities still remained. Elastic proton scattering on ^{4}He including the spin rotation parameter Q was also measured at a higher incident energy of 800 MeV [14]. At this energy, interactions should include the effects of Δ and π meson production. The authors mainly discussed the influence of Δ propagation on spin observables [14,15].

So far, microscopic analyses using realistic density distributions and NN interaction have been scarce for ^{4}He elastic scattering data. It is interesting to investigate how the high density of ^{4}He affects the observables of proton elastic scattering. In the present study, we want to elucidate the relationship between the density and proton elastic scattering in ^{4}He. The three observables $d\sigma/d\Omega$, A_y, and Q have been measured at 297 MeV for a wide range of angles from $\theta_{lab} = 12°$ to 66°. As beam energy, about 300 MeV has been chosen because there are parameter sets of NN interactions by Horowitz [2] which can be used in RIA calculations and because the effects of Δ and π meson production are negligible. The experimental procedure is described in Sec. II. The data reduction and the evaluation of experimental errors are presented in Sec. III. In Sec. IV experimental results are compared with calculations using the RIA of Horowitz. A detailed discussion of this comparison between the data and the calculations is given in Sec. V followed by a summary in Sec. VI.

II. EXPERIMENT

The experiment was performed at the Research Center for Nuclear Physics (RCNP), Osaka University. A polarized proton beam was accelerated up to 297 MeV [16] by the accelerator complex consisting of an AVF cyclotron and a ring cyclotron [17] and transported onto a liquid ^{4}He target in the scattering chamber. The cross section $d\sigma/d\Omega$ and analyzing power A_y were measured using a vertically polarized beam, and the spin rotation parameter Q was measured using a horizontally polarized beam. The protons scattered from ^{4}He were momentum analyzed by using the high-resolution magnetic spectrometer ''Grand Raiden'' [18] which is shown schematically in Fig. 1. Grand Raiden consists of two dipole magnets D1,D2, two quadrupole magnets Q1,Q2, a sextuple magnet SX, and a multipole magnet MP for the higher-order corrections. A special dipole magnet DSR at the end of sys-

tem is used to rotate the spin for the determination of all the horizontal spin components. The tracks of the scattered protons were determined using a system of multiwire drift chambers of vertical-drift type (VDCS) [19] placed along the focal plane of Grand Raiden. For the measurement of the spin rotation parameter Q, two independent in-plane polarizations of scattered protons were measured using the focal-plane polarimeter (FPP) system [20] and the DSR magnet [18]. The event trigger system consisted of a thin (3-mm) ΔE scintillator and two (X,Y) scintillator hodoscopes. The second-arm magnetic spectrometer ''LAS'' [21] was placed at a fixed angle on the other side, and was used as a monitor for the thickness of the liquid ^{4}He target by counting protons scattered elastically.

A. Polarized beam and beam line polarimeters

The polarized proton beam was produced by an atomic-beam-type polarized ion source with an ECR ionizer [22]. The polarization states (''up'' or ''down'') of the primary beam were periodically reversed with a frequency of 1 Hz. In the measurements of the cross section $d\sigma/d\Omega$ and analyzing power A_y, the beam intensity was measured with an internal Faraday cup [23] inside the scattering chamber. The beam current was adjusted from 0.1 nA to 2.0 nA with increasing scattering angle, and was limited by the data acquisition rate. In order to obtain a horizontally polarized beam for the measurement of Q, we used a superconducting solenoid located between the AVF cyclotron and the ring cyclotron which precessed the direction of polarization from the vertical axis to the horizontal. In the measurements of Q at angles larger than $\theta_{lab} = 22.5°$, the beam intensity was measured in a shielded external Faraday cup located about 30 m downstream of the target. The maximum beam intensity was about 30 nA.

During the measurements, the beam polarization was continuously monitored by two sets of beam line polarimeters. These polarimeters measured protons scattered at 17° from a $(CH_2)_n$ target in coincidence with the recoil protons by four detector sets placed up, down, left, and right relative to the beam direction. Each polarimeter was able to measure the vertical and horizontal components of the beam polarization.

Beam-bending dipole magnets were placed between these polarimeters with total bending angles of 50°, which caused a spin precession of 118.0° for 297 MeV protons relative to the beam direction. The three-dimensional polarization vector of the beam was determined with the polarization components measured in both polarimeters. The absolute value of the beam polarization was about 70% during the experiment. In the measurements of Q, the angle between the direction of the beam and polarization axis in the horizontal plane at the ^{4}He target was approximately 30°. The remaining vertical component of the beam polarization was about 0.03.

The value of 0.40 ± 0.01 was employed as the A_y of the $(CH_2)_n$ target used in the beam line polarimeters at 297 MeV, which is deduced from the A_y of p-p scattering after a small correction for the quasifree scattering from carbon. This value was calibrated by a low-energy beam polarimeter
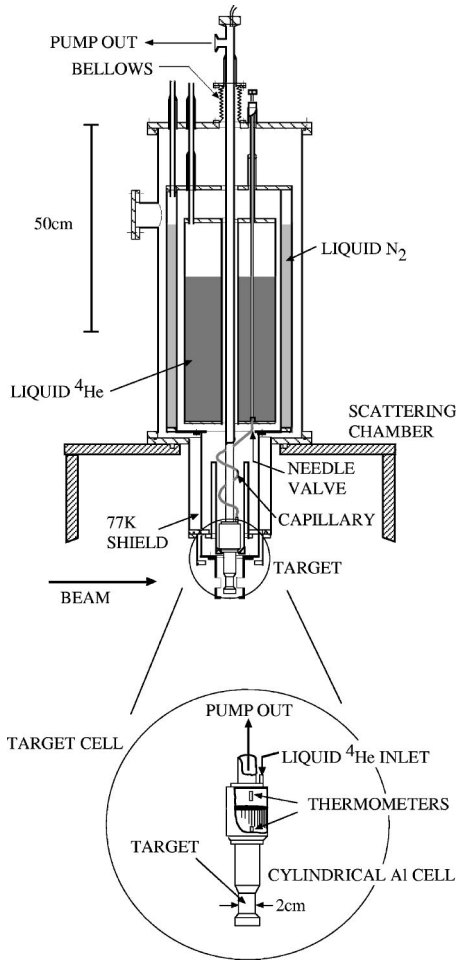
FIG. 2. Schematic cross sectional view of the liquid helium target and enlarged picture of the target.

located between the AVF and ring cyclotron assuming that the depolarization in the ring cyclotron was negligible. In the low-energy beam polarimeter, the asymmetry of elastically scattered protons from C at $E_p = 52.9$ MeV was measured at $\theta_{lab} = 50°$. The A_y for this polarimeter was well established in the previous work [24].

B. Liquid-helium target

A liquid-helium target [25] with a diameter of 19.6 mm was used in order to assure sufficient count rates even at backward angles where cross sections are small. A schematic view of the liquid-helium target system and an enlarged picture of the target is shown in Fig. 2. The system consists of three main parts: a liquid-nitrogen (N_2) reservoir, a liquid-helium (^{4}He) reservoir, and the target cell. The cylindrical target cell is made of aluminum with its axis in the vertical direction. The thickness of the cell wall which is penetrated by the beam is 0.2 mm. The cell diameter is 2.00 cm. The target cell is surrounded by a 77 K copper shield for thermal insulation.

The temperature of the liquid helium was measured by two thermometers installed 7 cm and 12 cm above the beam center inside the target cell. The upper thermometer is a Si diode and the lower one is a carbon resistor thermometer. In order to monitor the pressure inside the cell, a capacitance pressure transducer was installed near the pumping port at the top of the target system.

The liquid helium flowed into the target cell through a needle valve and a capillary at the bottom of the helium reservoir. After flowing into the target cell, helium evaporated due to the heat from the energy loss of the beam, thermal radiation, and thermal conduction. The evaporated helium gas was pumped out through the stainless steel pipe and the port.

By monitoring the temperature with the upper thermometer, helium gas inside the cell was often evacuated automatically with a rotary pump in order to keep the cell filled with liquid helium. The liquid-helium surface was kept above the lower thermometer. Since this evacuation continued periodically every few seconds, bubble formation inside the cell was avoided. The temperature of the liquid was set by adjusting the needle valve and was monitored with the lower thermometer. By adjusting the conductance in the evacuation line, the pressure inside the target cell was controlled.

C. Dipole magnet for spin rotation and focal-plane polarimeter

For the measurement of the spin rotation parameter Q, the dipole magnet for spin rotation (DSR magnet) placed downstream of the bending dipole magnet (D2) of Grand Raiden was used. The DSR magnet was operated with two deflection angles of $+18°$ and $-17°$. The spin precession angle (α) relative to the proton path after passing through the dipole field is

$$\alpha = \gamma(g/2 - 1)\psi, \quad \gamma = (1 - \beta^2)^{-1/2}, \tag{1}$$

where β is the velocity of the proton, $g = 5.586$ is the g factor of protons, and ψ is the deflection angle of the proton path. In our experiment, the kinetic energy of scattered protons changed between 211 MeV and 293 MeV depending on the scattering angles. The spin precession angle α is determined by both γ which is the function of the proton energy and the deflection angle either $+18°$ or $-17°$ of the DSR magnet. Therefore, the difference of the precession angle α for the two DSR modes varied between $77.6°$ and $82.9°$. Both the VDCS and FPP detector systems were mounted on a support which can be rotated according to the mode (DSR+ or DSR−) of the DSR magnet as shown Fig. 1.

After momentum analyses of the scattered protons by Grand Raiden and their position and angle measurements in the focal-plane detectors, the polarizations were measured by the FPP system. A schematic picture of the VDCS and the FPP system is shown in Fig. 3. The FPP system consists of a carbon analyzer C, two multiwire proportional counters MWPC-3 and MWPC-4, and two sets of plastic-scintillator hodoscopes PS-X and PS-Y. Each MWPC consists of three anode planes X-U-V with diagonal wire directions, i.e., $+45°$ and $-45°$ in the U and V anode wire planes, respectively. The anode wire spacing is 2 mm. In the experiment, only the U and V planes were used. The sensitive detector areas of MWPC-3 and MWPC-4 are 1400 mm × 418 mm
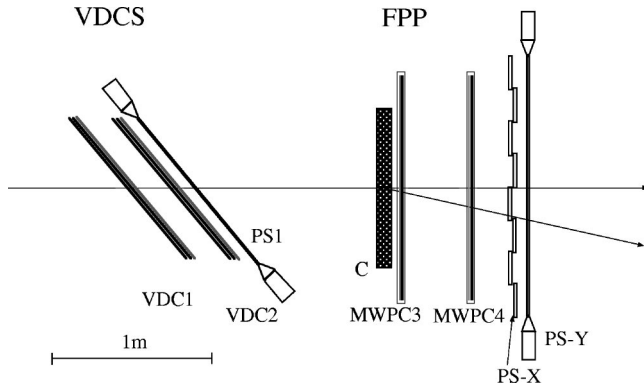
FIG. 3. Schematic layout of the focal-plane position detector system (VDCS) and the focal-plane polarimeter (FPP). The notation refers to vertical drift chambers (VDC), multiwire proportional chambers (MWPC), plastic scintillators (PS), and carbon analyzer (C).

and 1400 mm × 600 mm, respectively. The carbon analyzer C had a total thickness of 9 cm and was used as a secondary scattering target.

Up-down asymmetries of the protons scattered from the C target were measured with the FPP system in order to obtain polarizations in the scattering plane. Using the polarizations measured in both DSR modes, the spin rotation parameter Q can be determined as will be shown in Sec. III C. Left-right asymmetries were also measured in order to determine the vector polarization ($P_{y'}$) of the scattered protons. In order to decrease the trigger rates of the data taking system, small angle scattering events from the carbon analyzer, which have very small asymmetries, were eliminated by using a second-level trigger [26].

III. DATA REDUCTION AND RESULTS

A. Beam polarization

The polarization of the beam on target was monitored by two sets of beam line polarimeters during the measurement as described in Sec. II A. The vertical beam polarizations deduced from both polarimeters agreed within statistical errors and the nominal value was taken as an average of the results from both polarimeters. The horizontal components of the beam polarization were determined by combining measurements of both beam line polarimeters. With this method, the polarization and its direction on target were simultaneously calculated. The statistical error of the polarization was typically 0.015 and that for the direction of the horizontal beam polarization was less than 1.0°. The uncertainty of the normalization of the polarization came from the analyzing power of the CH$_2$ target as mentioned in Sec. II A.

B. Cross section and analyzing power

From the liquid ^{4}He target, the elastically scattered protons were momentum analyzed by Grand Raiden. A sample spectrum and a θ_p-E_p plot obtained from the VDCS are shown in Fig. 4. Since the background caused by a target cell
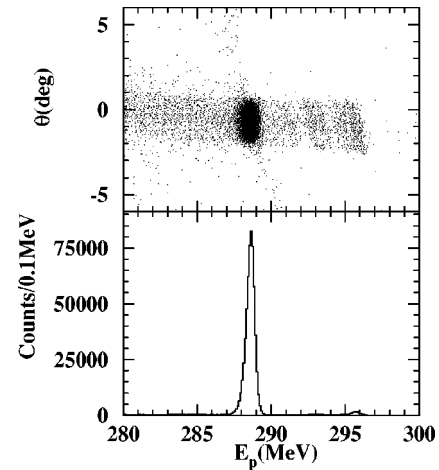

FIG. 4. Sample spectra of ^{4}He(p,p_0) elastic scattering at 18° measured in the focal plane of the Grand Raiden spectrometer. The upper panel shows a two-dimensional plot of energy vs the incident angle of particles relative to the central scattering angle. The lower panel shows the projection of the two-dimensional plot onto the energy axis. Counts in the large peak are elastic events. Some background events from the aluminum target cell can also be seen.

made of aluminum is sufficiently smaller than the elastic peak from ^{4}He, the elastic events are reliably deduced after background subtraction.

The number of elastic events for the beam spin up and down were used to calculate the cross section $d\sigma/d\Omega$ and analyzing power A_y. The number of the up- (down-) mode events was normalized with tracking efficiencies of the VDCS and the live time of the data acquisition system. A typical value of the tracking efficiency was about 80% which is somewhat dependent on the spin mode. The live time depended largely on the spin mode due to rate limitations of the data acquisition. In the measurement at 18° with large A_y, the difference between up and down modes was maximum. Here, the live time was 75% for the spin up mode and 90% for the spin down mode. Since the current integral module was less reliable at a beam current below 1 nA, the event number of beam line polarimeters was used for the relative normalization of the incident protons for all measurements. The uncertainty of this estimation was at most 3%. This number was normalized by the beam current over 1 nA.

The LAS spectrometer, which was used as a target thickness monitor, was set at fixed angles, either 31° for the backward measurements or 60° for the forward measurements. During the experiment, the target thickness of liquid ^{4}He target was constant within the statistical error of the LAS events. From the measured temperature and pressure of the liquid helium target, the density was determined 0.1265 ± 0.0015 g/cm^3.

The measured angular distributions for the $d\sigma/d\Omega$ and A_y are shown in Fig. 5 and Fig. 6 by solid circles. The error bars of $d\sigma/d\Omega$ contain uncertainties in the liquid target density and the statistical errors which are almost within the circles. The error bars of A_y contain the statistical errors. An overall normalization uncertainty of about 2.5% has to be added to the errors of A_y in the figure.
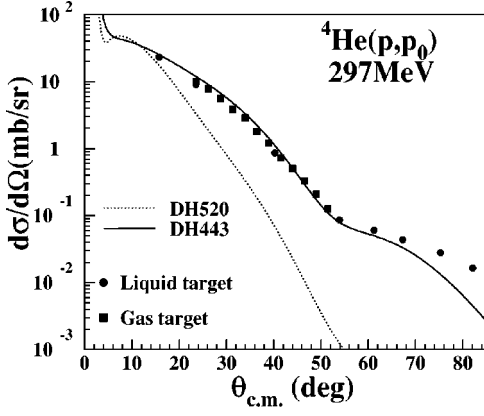
FIG. 5. Comparison between measured differential cross sections at 297 MeV incident proton energy and RIA calculations with Dirac-Hartree (DH) density distributions. The solid curve uses the DH443 distribution ($M_S = 443$ MeV/c^2) and the dotted curve the DH520 distribution ($M_S = 520$ MeV/c^2). Both the present liquid target data (circles) and the previous gas target data (squares) are plotted.

In Figs. 5 and 6, the A_y and $d\sigma/d\Omega$ data previously measured using the high-pressure gas target [27] are also plotted with solid squares. The new A_y data at forward angles ($6° \leqslant \theta_{lab} \leqslant 38°$) are consistent with our previous data. In that experiment the beam current was less than 1 nA. This value was below the sensitive range of the current digitizer and therefore the absolute normalization factor had a large ambiguity. For this purpose, we renormalized the $d\sigma/d\Omega$ data of the gas target by the liquid target data at 18°.

C. Spin rotation parameter Q and polarization $P_{y'}$

We measured the polarization transfer coefficients of the elastically scattered protons from the ^{4}He target by using the two DSR modes (DSR+, DSR−) for each scattering angle θ. The horizontal spin components of scattered protons precess in the vertical magnetic field of Grand Raiden and DSR. For example, at a scattering angle of $\theta = 42°$, the precession angles of the polarization axis relative to the proton's path were $\chi^+ = 410.9°$ and $\chi^- = 330.2°$ for the DSR+ and DSR− modes, respectively. The polarization vector of scattered protons was determined by measuring asymmetries after second scattering in the carbon analyzers of the FPP system. The transverse polarization component $p''_{x''}$ in the median plane is calculated using the up-down asymmetry ϵ:

$$p''_{x''} = \frac{\epsilon}{A_y^{eff}} = \frac{1}{A_y^{eff}} \frac{1-x}{1+x}, \quad x = \sqrt{\frac{D_\uparrow U_\downarrow}{U_\uparrow D_\downarrow}}, \qquad (2)$$

where A_y^{eff} is an effective analyzing power of the FPP system. The notation $U_\uparrow, U_\downarrow, D_\uparrow, D_\downarrow$ refers to the events for beam spin up ($\uparrow$) or down ($\downarrow$) measured in the FPP counter scattered up (U) or down (D). In these calculations, differences of efficiencies and solid angles between up (U) and down (D) measurements are canceled out. The spin rotation
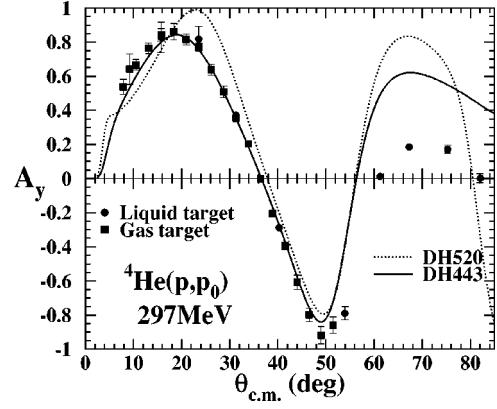

FIG. 6. Comparison between measured analyzing powers A_y and RIA calculations with DH density distributions. The notation is the same as that in Fig. 5.

angle β is defined as the rotation angle of the polarization direction in the scattering plane between initial and final states in the same coordinate system [28]. If we define $\chi^{+(-)}$ as the precession angle in the DSR+ (DSR−) mode with corresponding superscripts + (−), a relationship between β and $p''^{+(-)}_{x''}$ is expressed as follows:

$$p''^{+(-)}_{x''} = \frac{\epsilon^{+(-)}}{A_y^{eff}} = \frac{1}{A_y^{eff}} \frac{p_{xz}^{+(-)} \sqrt{1-A_y^2}}{1+A_y p_y^{+(-)}}$$

$$\times \cos(\beta - \theta_{lab} - \zeta + \chi^{+(-)} + \beta_0^{+(-)}), \qquad (3)$$

where $p_y^{+(-)}$, $p_{xz}^{+(-)}$ are the normal component, the in-plane component, and $\beta_0^{+(-)}$ is the angle of the direction of the beam polarization in the median plane (scattering plane). The quantities θ_{lab} and A_y are the scattering angle and the analyzing power of elastic scattering from ^{4}He. The definition
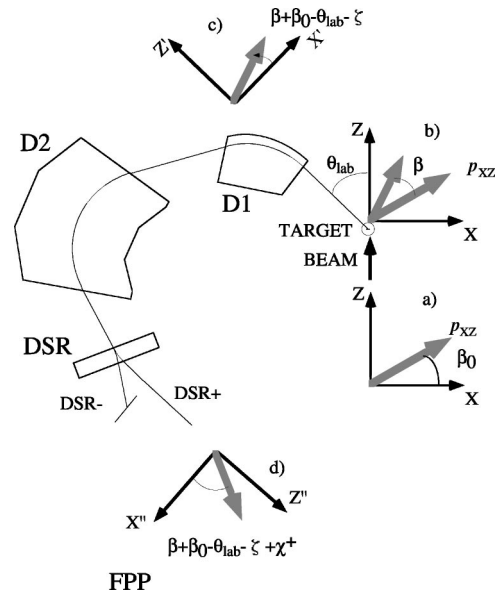

FIG. 7. Definition of the coordinate systems (X,Z), (X',Z'), and (X'',Z'') used in the deduction of the spin rotation parameters.

of the (X,Z) and (X'',Z'') coordinate system is indicated in Fig. 7. The description of the measurements on p_y and p_{xz} is presented in Sec. II A. The relativistic correction angle ζ comes from the change of the laboratory frame to the c.m.

$$\tan(\beta - \theta_{lab} - \zeta) = \frac{(1 + A_y p_y^-)p_{x''}^{''-} \cos(\chi^+ + \beta_0^+)/p_{xz}^- - (1 + A_y p_y^+)p_{x''}^{''+} \cos(\chi^- + \beta_0^-)/p_{xz}^+}{(1 + A_y p_y^-)p_{x''}^{''-} \sin(\chi^+ + \beta_0^+)/p_{xz}^- - (1 + A_y p_y^+)p_{x''}^{''+} \sin(\chi^- + \beta_0^-)/p_{xz}^+}. \quad (4)$$

In these calculations, A_y^{eff} is canceled out. This is important, because the energy of the scattered protons from ^{4}He varies and so does A_y^{eff}. The A_y^{eff} values were determined by solving simultaneously the above equations (3) and (4). In the experiment, for example, A_y^{eff} was 0.45 for an energy of scattered protons of 273 MeV at $\theta_{lab} = 36°$. The obtained A_y^{eff} values were consistent with the fitting parameters obtained by McNaughton *et al.* [30].

The spin rotation parameter Q is related with β by

$$Q = \sqrt{1 - A_y^2} \sin \beta. \quad (5)$$

To avoid the calculation of higher-order error propagation or correlations, the error for Q was estimated by Monte Carlo simulations assuming normal and Poisson distributions of directly measured values and their errors. The statistical errors of the value Q were less than 0.03 even at backward angles. The data points of Q are shown in Fig. 8. The uncertainty of Q from overall normalization errors of A_y is at most 0.02. The vector polarization $(P_{y'})$ was simultaneously obtained from the left-right asymmetry. For p-^{4}He scattering, $P_{y'}$ is equal to A_y as can be deduced from parity conservation. The measured $P_{y'}$ and A_y results are consistent within uncertainties.

IV. ANALYSIS WITH THE RELATIVISTIC IMPULSE APPROXIMATION

A. RIA model

For the present microscopic study, we calculated the observables with the relativistic impulse approximation using a program coded by Horowitz *et al.* [31]. In this RIA framework, the observables, especially the spin observables of heavier nuclei, have been well reproduced in the energy region from 200 MeV to 400 MeV [3]. We calculated p-^{4}He scattering using this RIA program and compared the calculated results with our experimental data.

In the RIA framework, the NN amplitudes $\hat{F}$ are represented by a set of Lorentz invariants i (S=scalar, V=vector, P = pseudoscalar, A = axial vector, and T = tensor):

$$\hat{F} = \sum_{i=S,V,P,A,T} \lambda_{(1)}^i \lambda_{(2)}^i F^i, \quad (6)$$

frame system [29]. For example the maximum value of ζ is 2.76° at $\theta_{lab} = 66°$. All angles are positive if the rotation is the same as that of scattered protons. The spin rotation angle β is determined by the equation

where the $\lambda_{(1)}^i, \lambda_{(2)}^i$ stand for the five Dirac operators corresponding to the above listed Lorentz invariants i. The labels 1 and 2 stand for protons of beams and nucleons in the target nuclei, respectively. The first-order Dirac optical potential for the spherical nuclei is produced by folding this NN amplitude with the target density:

$$U_{opt}(q) = \frac{-4\pi i p_{lab}}{M} [F^S(q)\rho_S(q) + \gamma^0 F^V(q)\rho_V(q)], \quad (7)$$

where q is the momentum transfer and the densities $\rho_i(q)$ are the Fourier transforms of the r-space scalar and vector densities. These are sums over the occupied nuclear levels:

$$\rho_S(r) = \sum_{\alpha}^{occupied} \bar{\phi}_\alpha \phi_\alpha, \quad \rho_V(r) = \sum_{\alpha}^{occupied} \phi_\alpha^\dagger \phi_\alpha, \quad (8)$$

where ϕ_α is the single-particle four-component wave function labeled by state α. Although a tensor term has to be included for a spin-zero nucleus, it is omitted because of its small contribution in the code. Thus the Dirac equation for the projectile is written as

$$\{-i\boldsymbol{\alpha}\cdot\boldsymbol{\nabla} + U^V(r) + \beta[M + U^S(r)]\}\mathcal{U}_0(\boldsymbol{x}) = E\mathcal{U}_0(\boldsymbol{x}), \quad (9)$$

where E is the total energy of the projectile in the proton-nucleus c.m. coordinates system and M the rest mass of the proton.
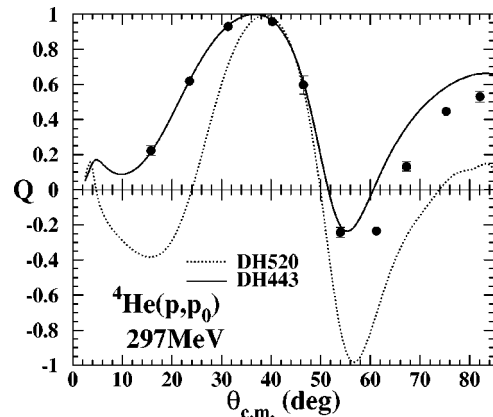

FIG. 8. Measured spin rotation parameters Q and RIA calculations. The notation is the same as Fig. 5.
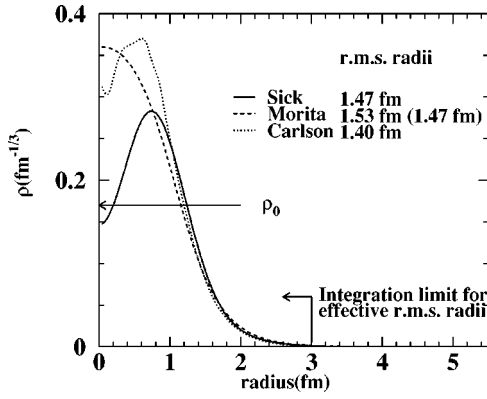
FIG. 9. Several vector density distributions of ^{4}He used in the RIA calculation. The solid curve (Sick) is the distribution obtained from the experimental charge distribution of ^{4}He by unfolding the charge form factor of a proton. The dotted curve and the dashed curve are Carlson's GFMC calculation and Morita's ATMS calculation, respectively. Neutron density distributions are assumed to be equal to the proton density distributions. ρ_0 indicates ''normal'' density.

For a free NN interaction, a meson parameter set of the relativistic Love-Franey (RLF) model is used, which takes into account the exchange of mesons in the first-order Born approximation including both the direct and exchange NN scattering diagrams [2]. Instead of a pseudoscalar invariant term, a pseudovector invariant term is chosen to alleviate the divergence of the potentials at lower energy. Parameter sets for 200 MeV, 300 MeV, and 400 MeV were reported by Murdock and Horowitz (MH) which were determined by fitting NN scattering data [1]. We used the MH parameter set for 300 MeV in the present calculations.

For both the scalar and the vector density distributions for ^{4}He, we used at first a result of Dirac-Hartree (DH) calculations [31]. In the original DH calculations, the scalar meson mass was chosen so as to reproduce the charge rms radius of ^{40}Ca. In this application of the DH calculation for ^{4}He—a light nucleus where the removal of the center-of-mass motion needs to be taken into account—we treated the scalar meson mass as a free parameter.

In addition to the DH density distributions, we also used three nonrelativistic baryon density distributions which are shown in Fig. 9. Two of the distributions are the results of microscopic calculations and the third is an empirical density distribution. The dashed line in Fig. 9 shows the ATMS calculation of Morita *et al.* [5] and the dotted line shows the GFMC calculation of Carlson [6]. The solid line denoted as ''Sick'' [4] shows the distribution which is obtained from experimental ^{4}He charge distribution by naively unfolding with the charge distribution of a free proton. In the RIA calculations with these nonrelativistic density distributions which have no scalar densities, we assumed that the shapes of scalar density distributions are the same as the nonrelativistic baryon (vector) density distributions:

$$\rho_S(r) = R_{SV} \times \rho_V(r). \tag{10}$$

As an initial value of this constant, we used the volume integral ratio of the DH densities as follows:

$$R_{SV} = \frac{\displaystyle\int_v \rho_S dv}{\displaystyle\int_v \rho_V dv}. \tag{11}$$

This selection will be discussed in more detail in the next section.

Since ^{4}He is a light nucleus, the recoil correction should be taken into account. Several methods of including the recoil effect have been suggested [32,33]. We examined the effect of the recoil correction, using the method of Cooper and Jennings [33]. Here, both the scalar and vector potentials (U^S, U^V) are multiplied by constants

$$U^S \rightarrow \frac{M_t c^2}{E_t + E_p} U^S, \quad U^V \rightarrow \frac{E_t}{E_t + E_p} U^V, \tag{12}$$

where E_t and E_p denote the total energy of target and proton in the c.m. system, and M_t denotes the rest mass of the target.

B. Comparison of experimental data with calculated results

At first, the observables were calculated without a recoil correction. In the DH calculation, Horowitz used the scalar meson mass (M_S) of 520 MeV/c^2 to reproduce the empirical charge rms radius of ^{40}Ca and this value gives an appropriate density distribution for most other nuclei. In the case of ^{4}He, this value gives a density distribution with a rms radius of 2.0 fm, which is much larger than the value deduced from the realistic density distributions shown in Fig. 9. Moreover, the $d\sigma/d\Omega$ obtained by RIA calculation does not reproduce the data at all (see the line labeled DH520 in Fig. 5). By decreasing the M_S in the DH calculations the rms radius is closer to the realistic rms radius and the calculated $d\sigma/d\Omega$ agrees much better with the data. With a value of $M_S = 443$ MeV/c^2, A_y and Q are well reproduced up to angles of about 40° as shown in Figs. 6 and 8 and the measured $d\sigma/d\Omega$ are reasonably reproduced by the calculation (see DH443 line in Fig. 5). The R_{SV} of the DH calculation is 0.92, and its rms radius is 1.34 fm.

In the RIA calculation with the various nonrelativistic density distributions, we employed the above value of $R_{SV} = 0.92$ to get scalar density distributions. The results are shown in Fig. 10. All calculations for the spin observables give almost the same results and reproduce well the experimental data at forward angles ($\theta_{c.m.} \lesssim 40°$) although the shapes of the density distributions are rather different. For the $d\sigma/d\Omega$, all calculations also explain the data at forward angles. For angles larger than 30°, however, the calculation with the Carlson density is slightly larger than the other calculations. At backward angles ($\theta_{c.m.} > 40°$), while three observables are very sensitive to the choice of the density distributions, all the calculated cross sections underestimate the experimental results.

Here, we consider the recoil correction in the RIA calculation. Figure 11 shows this effect on the observables when the correction of the Cooper-Jennings method is applied. The
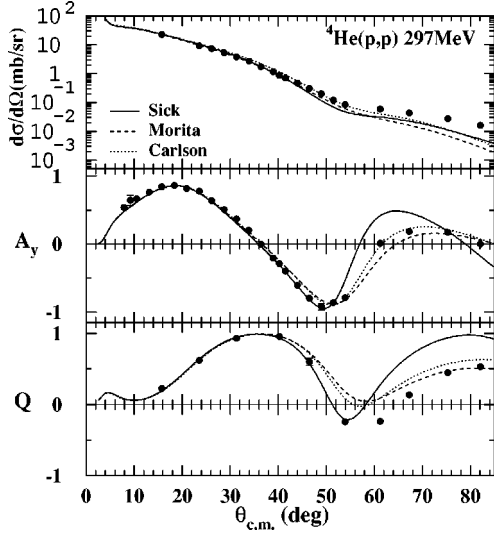
FIG. 10. Comparison between the experimental data and RIA calculations with nonrelativistic density distributions. The solid curve represents the results for the empirical distribution (Sick). The dotted curve shows the results using Carlson's GFMC distribution. The dashed curve shows the results using Morita's ATMS distribution. Mean values of the previous data with gas targets and the present data with the liquid ^{4}He target are represented for the data points at the same scattering angles.

reduction factors defined in Eq. (12) are 0.761 for the scalar potentials and 0.771 for the vector potentials. Although the absolute values of the potentials change by a large amount, the ratio of scalar to vector potentials is kept within 1%. While this correction decreases the cross section by 60%, it does not change spin observables much.

V. DISCUSSION

In the previous section, the experimental angular distributions of three observables were well reproduced by the RIA
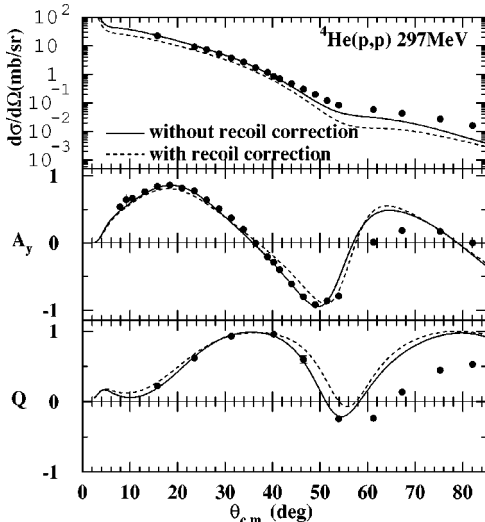

FIG. 11. Comparison between the data and RIA calculations with and without the recoil correction. The empirical distribution (Sick) is used as the density distribution.

at forward angles smaller than 40° irrespective of the choice of the model density. On the other hand, at backward angles larger than 40°, we cannot reproduce the cross section data. This may suggest the complexity of the reaction mechanism unexplained by the RIA. In the following four subsections, we will discuss the findings from a comparison of the experimental results and the RIA calculations at forward angles. In the last subsection, we will briefly discuss the discrepancies at backward angles.

A. Dirac-Hartree density distribution

In the RIA calculation, both vector and scalar densities are needed. The Dirac-Hartree approximation is a reasonable model to give these relativistic densities. The three calculated RIA observables, especially the spin observables using the DH density for ^{4}He, are in good agreement with the experimental data at forward angles when the value of M_S is reduced from the original 520 MeV/c^2 to 443 MeV/c^2. The density distribution obtained with the value of M_S = 443 MeV/c^2 showed a realistic baryon density distribution for the ^{4}He nucleus, the rms radius of which is about 1.4 fm, so that the central density is twice as high as the ''normal'' density. In the DH calculation of Horowitz *et al.*, M_S was treated as a parameter which mainly determine the rms radius of the nucleus. The rms radius of the nucleus decreases by reducing the value of M_S. Horowitz *et al.* chose 520 MeV/c^2 so that the empirical rms radius of ^{40}Ca was reproduced. This value was successfully applied in the wide mass number region from ^{12}C to ^{208}Pb. However, we again treated M_S as a free parameter to account for the center-of-mass motion of such a light nucleus as ^{4}He. It is surprising that a realistic density of ^{4}He is obtained only by the large reduction of M_S from 520 MeV/c^2 to 443 MeV/c^2, because the DH approximation, which is ''mean field'' theory, is thought to be difficult to apply for the four-nucleon system. On the other hand, R_{SV} of the ^{4}He density also decreases as reducing M_S. The DH density with $M_S = 520$ MeV/c^2 has R_{SV} of 0.98 and that with $M_S = 443$ MeV/c^2 has R_{SV} of 0.92. This small R_{SV} mainly contributes to reproducing the experimental spin observables as discussed in detail in the next subsection.

B. R_{SV} and spin observables

We have employed various nonrelativistic or relativistic DH models to describe the target nuclear densities. For the nonrelativistic densities we assumed that the scalar and vector density distributions are identical. Hence, the only free parameter is the ratio R_{SV} of the scalar to vector density. As a starting value, we adopted $R_{SV} = 0.92$ which was the best result of the DH calculations. In the relativistic case the scalar and vector densities are different.

We calculated the angular distributions for each observable by changing R_{SV} and found that the spin observables A_y and Q are very sensitive to R_{SV}. In order to determine the best R_{SV}, we calculated the reduced χ^2 values for spin observables by varying R_{SV} not only for a nonrelativistic (Sick) but also relativistic DH densities. The experimental data in the angular range $\theta_{c.m.} \leq 40°$ was included in the fit. It should

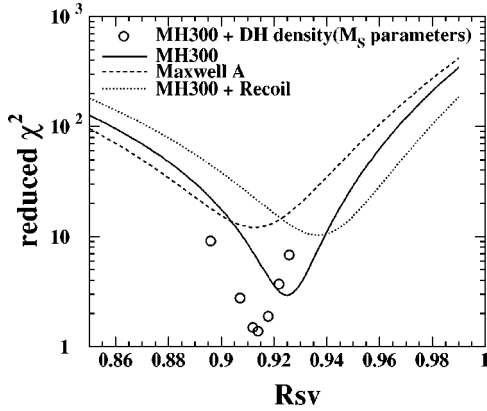FIG. 12. Graph of the reduced χ^2 for spin observables as a function of the ratio of scalar to vector density R_{SV}. The solid curve uses the parameter sets of Murdock and Horowitz at 300 MeV. The dashed curve uses the parameter set A of Maxwell. Results with the recoil correction are plotted by the dotted curve. On all curves, the empirical density distribution (Sick) is used. Open circles show the results with DH density distributions.

be noted that in the DH calculation, the primary parameter is M_S which gives the corresponding R_{SV} value. The solid curve in Fig. 12 is the result of the nonrelativistic density (Sick) while open circles represent the result of the relativistic one (DH). The best value for R_{SV} is 0.925 in the former case and 0.915 in the latter. The small difference is mainly due to the discrepancy of the angular distributions at medium angles. When using the other nonrelativistic densities, we obtained a best R_{SV} at the very similar value of 0.92. Around the best R_{SV} value, the $d\sigma/d\Omega$ data are also reproduced. We conclude that the experimental data for a ^{4}He data set are well reproduced by the RIA with the common value of R_{SV} (≈ 0.92), irrespective of the choice of density model if only forward angles are considered. This conclusion is in contrast to the results obtained for heavier targets, e.g., ^{16}O, ^{40}Ca, and ^{208}Pb, in which R_{SV} values are 0.96–0.98. A sizable difference of R_{SV} between ^{4}He and heavier nuclei is considered to indicate that the ^{4}He nuclear density is much higher than those for heavier elements. It was reported that in nuclear matter calculations the ratio of the scalar to vector densities decreases with increasing density [34]. When we calculate the scalar density distribution from realistic ^{4}He density by applying the density-dependent ratio of scalars to vectors from the nuclear matter calculation, the ratio of the volume integral R_{SV} takes a value of about 0.92. If we apply the same procedure to ^{40}Ca, a R_{SV} of 0.95 is obtained.

C. rms radii and cross sections

In this subsection, we discuss the relationship between the density distribution and the cross section $d\sigma/d\Omega$. The rms radii of the four density distributions are 1.40 fm, 1.47 fm, 1.53 fm, and 1.34 fm for the GFMC distributions, the unfolded distribution from the electron data, the ATMS distribution, and the DH distribution (DH443), respectively. The RIA calculations using all these density distributions reproduced the spin observables at forward angles with the same R_{SV} value of 0.92. As for the $d\sigma/d\Omega$ at forward angles, the

Sick and ATMS distributions are preferable. The ATMS density distribution has an unphysical large tail which results in a large rms radius. If we omit the tail region ($r > 3.0$ fm) which does not affect the observables, the rms radius has to be reduced to 1.47 fm. With this rms value of about 1.47 fm, the ^{4}He density distribution describes the observables well. However, it should be noted that we have assumed the same shape of the scalar and the vector density distributions for the nonrelativistic case. When the DH density which is different for the scalar and vector density distributions is used in the calculation so that only $d\sigma/d\Omega$ is much better reproduced, a rms radius of 1.40 fm is obtained. In the calculation with DH density distributions, $d\sigma/d\Omega$ was found to be very sensitive to the rms radius of the density distribution. In order to determine the rms radius conclusively, we need to know the exact shape of the scalar density distribution.

D. Recoil correction and NN interaction

In Fig. 11, it is shown that the RIA calculations with the recoil correction based on the method of Cooper and Jennings worsen the agreement with the data, especially for the cross section $d\sigma/d\Omega$. Although the spin observables are not so much affected mainly due to the rather small change (1%) of R_{SV}, the χ^2 value is about 3 times larger than without the recoil correction (see Fig. 12). If we search for a χ^2 minimum with the recoil correction, the best fit R_{SV} is slightly changed to 0.935 but the value of χ^2 is not much reduced. Why the RIA calculation without a recoil correction can better reproduce the data for such a light nuclei as ^{4}He is still an open problem.

Murdock and Horowitz indicated the importance of a correction arising from Pauli blocking [3], which causes a density dependence of the NN interaction. We performed calculations including this correction for ^{4}He. The agreement with the data, however, becomes worse in particular for the spin observable Q. Since ^{4}He consists of only four nucleons, this correction does not seem to be needed.

In the calculation above, we used the parameter sets of 300 MeV by Murdock and Horowitz for relativistic NN interaction. Maxwell recently gave another parameter set as a function of the beam energy [35]. Calculations with this interaction make the agreement with the data up to about 45° scattering angles worse as compared to the result with the interaction of MH. The reduced χ^2 value for the spin observables for this case is also plotted in Fig. 12. The calculated $d\sigma/d\Omega$ using the Maxwell interaction is larger by a factor of 1.2 than that with the MH interaction. The best fit R_{SV} is slightly decreased by about 0.1; however, the difference of the reduced χ^2 values between 0.91 and 0.92 of R_{SV} is small. The best fit R_{SV} value seems to be independent of the choice of NN interaction.

E. Behavior at backward angles

A comparison of the RIA calculation with the different nonrelativistic density distributions as presented in Fig. 10 shows that the shape differences of the distributions, particu-

larly in the central region, cause differences for the spin observables at backward angles. The behavior of density distributions in the central region affects the observables at backward angles. It may be possible to find density distributions where both spin observables are reproduced. However, we could not enlarge the calculated cross sections $d\sigma/d\Omega$ at backward angles to reproduce the measured $d\sigma/d\Omega$ with any reasonable density distributions.

In the analyses [13] of data measured at 500 MeV, Kobos *et al.* reported that the backward angle data $d\sigma/d\Omega$, A_y, and R can be reproduced by using a phenomenological scalar and vector potential which had minima in the central region. They suggested that this minimum might be caused by a central minimum in the ^{4}He point nucleon density (Sick) [4]. In fact, the point proton density distribution which is deduced from unfolding the electron scattering data has a minimum in the centers. However, this minimum in the potential becomes very shallow or disappears in the process of folding the free NN interaction with the density distribution. Although the cross sections calculated with the Sick density are slightly larger at backward angles, this increase is not sufficient to reproduce the data. For high momentum transfer, we may need to consider the complexity of the reaction mechanism not included in the RIA model.

VI. SUMMARY

We have measured angular distributions of cross sections $d\sigma/d\Omega$, analyzing powers A_y, and spin rotation parameters Q for proton elastic scattering on a ^{4}He target at 297 MeV. Precise data for all three quantities were obtained up to $\theta_{lab}=66°$ using the Grand Raiden spectrometer with the spin rotation magnet DSR, the focal plane polarimeter system FPP, and a liquid helium target. Microscopic analyses have been performed with the relativistic impulse approximation according to the prescriptions of Murdock and Horowitz. A realistic ^{4}He density distribution was obtained with the Dirac-Hartree approximation with scalar meson mass $M_S=443$ MeV/c^2. Using these RIA calculations, the forward angle data ($\theta_{\text{c.m.}}\leq40°$) are well reproduced. The ratio of the volume integral of the scalar to vector density R_{SV} is well determined. The ratio 0.92 obtained for ^{4}He is significantly smaller than those for heavier nuclei. This value is not affected by the selection of the NN interaction. Such a small value for R_{SV} is considered to indicate the existence of a higher nuclear density of ^{4}He compared to heavier nuclei. The calculated $d\sigma/d\Omega$ is sensitive to the rms radius of baryon (vector) density distributions. An rms radius of about 1.47 fm is preferable although it depends on the scalar density distribution. At backward angles, where the measured angular distributions show a second bump, all calculated cross sections based on RIA calculations underestimate the data while the spin observables are rather sensitive to the central region of the density distributions.

[1] R. A. Arndt, I. I. Strakovsky, and R. L. Workman, Phys. Rev. C **50**, 2731 (1994); **62**, 034005 (2000).

[2] C. J. Horowitz, Phys. Rev. C **31**, 1340 (1985).

[3] D. P. Murdock and C. J. Horowitz, Phys. Rev. C **35**, 1442 (1987).

[4] I. Sick, Phys. Lett. **116B**, 212 (1982); J. S. McCarthy, I. Sick, and R. R. Whitney, Phys. Rev. C **15**, 1396 (1977).

[5] H. Morita, Y. Akaishi, O. Endo, and H. Tanaka, Prog. Theor. Phys. **78**, 1117 (1987).

[6] J. Carlson, Phys. Rev. C **38**, 1879 (1988). Numerical values are taken from http://www.lanl.gov/~carlson

[7] A. W. Stetz, J. M. Cameron, D. A. Hutcheon, R. H. McCamis, C. A. Miller, G. A. Moss, G. Roy, J. G. Rogers, C. A. Goulding, and W. T. H. van Oers, Nucl. Phys. **A290**, 285 (1977); G. A. Moss *et al.*, Phys. Rev. C **21**, 1932 (1980).

[8] H. Courant *et al.*, Phys. Rev. C **19**, 104 (1979).

[9] L. G. Arnold, B. C. Clark, and R. L. Mercer, Phys. Rev. C **19**, 917 (1979).

[10] L. Wolfenstein, Phys. Rev. **96**, 1654 (1954); R. J. Glauber and P. Osland, Phys. Lett. **80B**, 401 (1979).

[11] G. A. Moss, C. A. Davis, J. M. Greben, L. G. Greeniaus, G. Roy, J. Uegaki, R. Abegg, D. A. Hucheon, C. A. Miller, and W. T. H. van Oers, Nucl. Phys. **A392**, 361 (1983).

[12] J. M. Greben and R. Gourishankar, Nucl. Phys. **A405**, 445 (1983).

[13] A. M. Kobos, E. D. Cooper, J. R. Rook, and W. Haider, Nucl. Phys. **A435**, 677 (1985).

[14] M. Geso, D. Adams, J. Bysterisky, G. Igo, A. Ling, C. Whitten, M. Nasser, L. C. Smith, and R. W. Whitney, Phys. Rev. C **58**, 3742 (1998).

[15] J. P. Auger and C. Lazard, J. Phys. G **16**, 1637 (1990).

[16] T. Noro, K. Hatanaka, K. Hosono, H. Akimune, H. Sakaguchi, M. Yosoi, A. Tamii, and S. Toyama, RCNP Annual Report, 1993, p. 167.

[17] I. Miura *et al.*, RCNP Annual Report, 1991, p. 149.

[18] M. Fujiwara *et al.*, Nucl. Instrum. Methods Phys. Res. A **422**, 484 (1999).

[19] T. Noro *et al.*, RCNP Annual Report, 1991, p. 177.

[20] M. Yosoi *et al.*, in *High Energy Spin Physics*, edited by K. J. Heller and S. Smith, AIP Conf. Proc. No. 343 (AIP, New York, 1995), p. 157; M. Yosoi *et al.,* RCNP Annual Report, 1994, p. 147.

[21] N. Matsuoka, T. Noro, K. Sagara, S. Morinobu, A. Okihana, and K. Hatanaka, RCNP Annual Report, 1992, p. 174.

[22] K. Hatanaka, K. Takahisa, H. Tamura, M. Sato, and I. Miura, Nucl. Instrum. Methods Phys. Res. A **384**, 575 (1997).

[23] H. Sakaguchi *et al.*, Phys. Rev. C **57**, 1749 (1998).

[24] M. Ieiri *et al.*, Nucl. Instrum. Methods Phys. Res. A **257**, 253 (1987).

[25] M. Yoshimura, M. Nakamura, M. Yosoi, M. Itoh, K. Yonehara, and H. Sakaguchi, RCNP Annual Report, 1996, p. 146.

[26] A. Tamii, H. Sakaguchi, H. Takeda, M. Yosoi, H. Akimune, M. Fujiwara, H. Ogata, M. Tanaka, and H. Togawa, IEEE Trans. Nucl. Sci. **43**, 2488 (1996).

[27] M. Yoshimura, S. Yamamura, S. Kuwamoto, M. Nakamura, Y. Sakemi, H. Akimune, A. Yamagoshi, M. Yosoi, H. To-gawa, and T. Noro, RCNP Annual Report, 1992, p. 48.

[28] G. G. Ohlsen, Rep. Prog. Phys. **35**, 717 (1972).

[29] R. D. Sard, *Relativistic Mechanics* (Benjamin, New York, 1970).

[30] M. W. McNaughton *et al.*, Nucl. Instrum. Methods Phys. Res. A **241**, 435 (1985).

[31] C. J. Horowitz *et al.*, *Computational Nuclear Physics 1* (Springer-Verlag, New York, 1991), Chap. 7.

[32] N. A. Ottenstein, J. Sabutis, and S. J. Wallace, Phys. Rev. C **35**, 369 (1987).

[33] E. D. Cooper and B. K. Jennings, Nucl. Phys. **A483**, 601 (1988).

[34] B. D. Serot and J. D. Walecka, Adv. Nucl. Phys. **16**, 1 (1986).

[35] O. V. Maxwell, Nucl. Phys. **A600**, 509 (1996).